The Astrophysical Journal, 937:51 (10pp), 2022 October 1 https://doi.org/10.3847/1538-4357/ac8c35

Possible Explosive Dispersal Outflow in IRAS 16076-5134 Revealed with ALMA

Estrella Guzmán Ccolque[1], Manuel Fernández-López[1], Luis A. Zapata[2], and Tapas Baug[3]
[1] Instituto Argentino de Radioastronomía (CCT- La Plata, CONICET,CICPBA), C.C. No. 5,1894, Villa Elisa, Buenos Aires, Argentina; estreguzman@gmail.com
[2] Instituto de Radioastronomía y Astrofísica. Universidad Nacional Autónoma de México, P.O. Box 3-72,58090, Morelia, Michoacán, México
[3] S.N. Bose National Centre for Basic Sciences, Block-JD, Sector-III, Salt Lake, Kolkata 700106, India
Received 2022 February 16; revised 2022 August 19; accepted 2022 August 22; published 2022 September 27

Abstract

We present 0.9 mm continuum and CO(3–2) line emission observations retrieved from the Atacama Large Millimeter/submillimeter Array archive toward the high-mass star formation region IRAS 16076-5134. We identify 14 dense cores with masses between 0.3 and 22 $M_\odot$. We find an ensemble of filament-like CO(3–2) ejections from −62 to +83 km s^{-1} that appear to arise radially from a common central position, close to the dense core MM8. The ensemble of filaments has a quasi-isotropic distribution in the plane of the sky. The radial velocities of several filaments follow a linear velocity gradient, increasing from a common origin. Considering the whole ensemble of filaments, we estimate the total mass to be 138 and 216 $M_\odot$, from its CO emission, for 70 K and 140 K, respectively. Also, assuming a constant velocity expansion for the filaments (of 83 km s^{-1}), we estimate the dynamical age of the outflowing material (3500 yr), its momentum ($\sim 10^4\ M_\odot$ km s^{-1}), and its kinetic energy ($\sim 10^{48-49}$ erg). The morphology and kinematics presented by the filaments suggest the presence of a dispersal outflow with explosive characteristics in IRAS 16076-5134. In addition, we make a raw estimate of the lower limit of the frequency rate of the explosive dispersal outflows in the galaxy (one every 110 yr), considering a constant star formation rate and efficiency, with respect to the galactocentric radius of the galaxy. This may imply a comparable rate between dispersal outflows and supernovae (approximately one every 50 yr), which may be important for the energy budget of the and the link between dispersal outflows and high-mass star formation.

Unified Astronomy Thesaurus concepts: Interferometers (805); Star formation (1569); Submillimeter astronomy (1647); Interstellar dynamics (839)

1. Introduction

IRAS 16076-5134 or AGAL 331.28-00.19 (hereafter, I16076) is an ultracompact HII (UCHII) region located at 5.0 ± 0.7 kpc (Baug et al. 2020; the kinematic distance is calculated using the "Kinematic Distance Calculation Tool" of Wenger et al. 2018). This measure is similar to the value obtained previously by Faúndez et al. (2004 derived using a flat rotation model of the Milky Way and the CS(2–1) line velocity reported by Bronfman et al. (1996). I16076 has a far-IR color typical of UCHII regions (Wood & Churchwell 1989). Faúndez et al. (2004) detected its dust emission at 1.2 mm, measuring its size (38″), dust temperature (33 K), and millimeter–IR bolometric luminosity ($2.0 \times 10^5\ L_\odot$). Such a large millimeter–IR bolometric luminosity in a cold dust region usually implies its link with a region forming one or more stars of spectral types B and O. A dense clump (radius = 1.57 pc) in I16076 was also observed in the ATLASGAL survey at 870 μm, for which Urquhart et al. (2018) presented values of H_2 column density (23.3×10^{15} cm^{-2}), mass (45.6 $M_\odot$), and dust temperature (30.1 K). In addition, they used a combination of archival observations from molecular line surveys reported in the literature (such as CO, NH_3, CS, etc.) to determine the radial velocity with regard to the LSR (v_{lsr}): −87.7 km s^{-1}. I16076 shows a strong blueshifted emission profile of HCN(4–3), known to be a tracer of infalling gas and therefore an indicator of accretion processes (Liu et al. 2016). More recently, I16076 was observed with the Atacama Large Millimeter/submillimeter Array (ALMA) at 3 mm in order to explore the molecular outflows in this region Liu et al. (2020). Baug et al. (2020) detected several outflow lobes in CO(3–2) toward I16076. Most of them are associated with the millimeter sources identified by Baug et al. (2021). In particular, from the dense core identified as I16076_O1, 19 outflow lobes seem to arise (9 redshifted and 10 blueshifted), distributed almost isotropically. This morphology is reminiscent of the dispersal outflows with explosive features detected in Orion BN/KL, DR21, and G5.89-0.39 (Bally et al. 2015, 2017; Zapata et al. 2017, 2019, 2020). Hereafter, we refer to these types of outflows as "explosive dispersal outflows" or just "dispersal

Since their discovery, explosive dispersal outflows have become a new subclass of molecular outflows observed in the star-forming regions of massive stars (e.g., Zapata et al. 2009). At present, there seem to be two types of molecular outflows. The first type comprises the classical outflows, which are typically bipolar, produced mostly by low-mass stars in their formation processes (Arce et al. 2007). Theoretical work suggests that these outflows are intimately related to the accretion process, play an important role in dissipating excess angular momentum in the infalling material, and allow the star to build up its mass through accretion (e.g., Shu et al. 1987, 1991; Konigl & Pudritz 2000; Shu et al. 2000). On the other side, there are the dispersal outflows with explosive characteristics, whose nature is still unknown (Bally & Zinnecker 2005; Zapata et al. 2009; Bally et al. 2011, 2017). These have been associated with energy releases produced by the disintegration or close encounters of young stellar systems (Bally et al. 2017; Rivera-Ortiz et al. 2021) or mergers of several massive protostars (Bally & Zinnecker 2005). These outflows appear to be impulsive and created by a single brief

Table 1
Summary of the Band 7 ALMA Observations of I16076 (Project 2017.1.00545.S)

Execution Block IDs	uid://A002/Xcda49e/Xb713	uid://A002/Xcda49e/Xc0a3	uid://A002/Xcdb7b8/Xd8c8
Observation Date	2018-05-21	2018-05-21	2018-05-23
Number of Antennas	48	48	45
Time on Source (s)	428.2	428.3	428.2
Mean PWV (mm)	0.4	0.5	0.3
Phase Calibrator	J1650-5044	J1650-5044	J1650-5044
Bandpass Calibrator	J1427-4206	J1427-4206	J1517-2422
Flux Calibrator	J1427-4206	J1427-4206	J1517-2422

energetic event, with energy injections of about $10^{47\text{-}49}$ erg (Bally & Zinnecker 2005). They comprise dozens of filament-shaped ejections that are isotropically distributed on the sky. Each filament follows a well-defined Hubble velocity law; that is, the radial velocities increase linearly with the projected distance (Zapata et al. 2009, 2013; Bally et al. 2017; Zapata et al. 2019). Dispersal outflows are usually detected by their CO emission (Peng et al. 2012; Zapata et al. 2017, 2019, 2020), but they have also been detected in H_2 (Bally et al. 2011), and [FeII] condensations have been observed at the tips of the filaments in the case of Orion BN/KL (Bally et al. 2015).

Zapata et al. (2017) enumerated four clear morphological and kinematical features of explosive dispersal outflows that distinguish them from classical bipolar molecular outflows:

1. The explosive dispersal outflows consist of straight narrow filament-like ejections with different orientations and an almost isotropic distribution.
2. The filaments point back to a common position where the explosive event may have occurred.
3. The radial velocity of each filament increases linearly with the distance projected on the sky from the origin; it seems to follow the Hubble law.
4. The redshifted and blueshifted filaments seem to overlap in the plane of the sky.

Moreover:

1. These outflows are associated with regions of high-mass star formation.
2. Their energies are in the range of $10^{47} - 10^{49}$ erg.

Using observations from the ALMA archive, and following the features of explosive dispersal outflows described in (Zapata et al. 2017), we propose the possible presence of this type of event in I16076. We reanalyze the dust and line kinematics of the ALMA data under this hypothesis, and present the new implications of the discovery. The paper is organized as follows. In Section 2, we present the ALMA observations. The identification and derivation of the physical parameters of the 0.9 mm continuum sources, as well as the CO(3–2) filamentary ejections, are presented in Section 3. A brief discussion about whether I16076 is an explosive dispersal outflow, and the rate of such events in the galaxy, can be found in Section 4. The conclusions of this study are presented in Section 5.

2. ALMA Observations

The Band 7 observations were carried out during ALMA Cycle 5, as part of the program 2017.1.00545.S (P.I: Liu Tie) Liu). The array was in C43-2 configuration, with 48 12 m antennas available at the time, and a baseline range of 15–314 m. The I16076 data presented in this article correspond to a portion of a larger program, comprising 10 more sources. I16076 was observed in three sessions (Table 1) during 2018 May, totaling approximately 21 minutes on source under good weather conditions, with precipitable water vapor (PWV) around 0.4 mm. The observations were made in mosaic mode, with 17 pointings covered during each individual session. The coordinates of the mosaic center were $(\alpha, \delta)_{J2000.0} = 16^{\rm h}11^{\rm m}27\overset{\rm s}{.}1, -51°41'55\overset{''}{.}1$.

The correlator was configured to use four spectral windows, centered at 343.302, 345.183, 354.505, and 356.840 GHz. The first two windows were used to image the continuum and the ^{12}CO(3–2) emission, respectively; they had a 0.976 MHz spectral resolution and a total bandwidth of 1.875 GHz. The last two spectral windows were aimed at the HCN(4–3) and HCO(4–3) lines; they had a 0.244 MHz (0.85 km s^{-1} at the observing frequency) spectral resolution and a total bandwidth of 0.469 GHz. In this work, we focus on the 0.9 mm continuum and the CO(3–2) line emission. J1650-5044 was used as the phase calibrator, while J1427-4206 and J1517-2422 were used as the bandpass and flux calibrators. The estimation of the absolute flux calibration for ALMA at these frequencies is ∼10%.[4]

The visibility data were reduced using the CASA 5.1.1 (Common Astronomy Software Applications) package. First, the data were calibrated by running the calibration script provided by the ALMA staff. The images were constructed using the *tclean* task of CASA version 6.1.2. The cleaning process was performed interactively, by applying the Hogbom minor cycle algorithm and Briggs weighting and by setting the robust parameter to 0.5, which ensures a good compromise between the sensitivity and the angular resolution of the images. The rms of the continuum image is 1.3 mJy beam^{-1} and the angular resolution is $0\overset{''}{.}8 \times 0\overset{''}{.}7$ (PA = 74°.6, where PA is the position angle).[5] For the CO cube, the rms is 5.6 mJy beam^{-1} per channel and the angular resolution is $0\overset{''}{.}9 \times 0\overset{''}{.}8$ (PA = 80°.6).

3. Results

3.1. Submillimeter Continuum Sources

Figure 1 shows the positions of 14 0.9 mm continuum sources detected with ALMA in I16076. These sources are labeled as MM sources and are sorted by their R.A. We consider a flux density threshold of $5\sigma \sim 7$ mJy beam^{-1} as a criterion for visually identifying continuum peaks, which we associate with continuum sources (here, σ is estimated by analyzing the empty background emission). The continuum

[4] See Section 10.4.7 in the ALMA Cycle 8 Technical Handbook.
[5] The PA is the measured angle of the beam's major axis with respect to the north celestial pole, turning positive in the R.A. direction (i.e., toward the east).

Table 2
Submillimeter Continuum Sources in I16076

Source	R.A. (ICRS)	Decl. (ICRS)	Deconvolved Size ($'' \times ''$, °)	Peak Intensity (mJy beam^{-1})	Flux Density (mJy)	Mass ($M_\odot$)	Name Baug
MM1	16:11:27.758 ± 0.008	−51:41:55.01 ± 0.03	3.8 ± 0.2 × 1.10 ± 0.06, 77 ± 1	4.0 ± 0.2	38 ± 2	2.9 ± 0.1	I16076_O3
MM2	16:11:27.668 ± 0.008	−51:41:51.71 ± 0.07	1.4 ± 0.2 × 1.1 ± 0.2, 50 ± 70	2.5 ± 0.3	9 ± 1	0.7 ± 0.1	⋯
MM3	16:11:27.660 ± 0.001	−51:41:55.57 ± 0.01	0.87 ± 0.01 × 0.70 ± 0.05, 50 ± 20	26.5 ± 0.7	56 ± 2	4.3 ± 0.2	I16076_O3
MM4	16:11:27.120 ± 0.002	−51:41:46.66 ± 0.05	1.5 ± 0.1 × 0.5 ± 0.2, 176 ± 3	2.2 ± 0.1	5.7 ± 0.5	0.44 ± 0.04	⋯
MM5	16:11:26.870 ± 0.007	−51:41:55.99 ± 0.07	1.5 ± 0.2 × 0.9 ± 0.2, 40 ± 20	5.2 ± 0.6	18 ± 2	1.4 ± 0.2	I16076_O4
MM6	16:11:26.626 ± 0.009	−51:41:49.85 ± 0.08	1.7 ± 0.3 × 0.9 ± 0.2, 50 ± 10	3.2 ± 0.4	12 ± 2	0.9 ± 0.1	⋯
MM7	16:11:26.550 ± 0.001	−51:41:59.48 ± 0.01	1.36 ± 0.03 × 1.11 ± 0.03, 162 ± 6	18.2 ± 0.3	69 ± 2	5.3 ± 0.1	I16076_O1
MM8	16:11:26.546 ± 0.005	−51:41:57.23 ± 0.06	1.6 ± 0.2 × 1.1 ± 0.1, 20 ± 10	70.4 ± 6.0	290 ± 30	22 ± 1	I16076_O1
MM9	16:11:26.5392 ± 0.0003	−51:41:55.820 ± 0.006	2.27 ± 0.01 × 0.981 ± 0.008, 178.1 ± 0.3	18.5 ± 0.1	101.1 ± 0.7	5.7 ± 0.3	I16076_O1
MM10	16:11:26.474 ± 0.004	−51:41:52.64 ± 0.03	2.1 ± 0.1 × 1.11 ± 0.06, 58 ± 3	13.9 ± 0.6	74 ± 3	5.7 ± 0.3	⋯
MM11	16:11:26.222 ± 0.008	−51:41:57.27 ± 0.03	point source	5.6 ± 0.4	7 ± 1	0.54 ± 0.08	⋯
MM12	16:11:26.12 ± 0.01	−51:41:59.62 ± 0.04	1.1 ± 0.3 × 0.4 ± 0.2, 100 ± 10	2.2 ± 0.3	4 ± 1	0.31 ± 0.06	⋯
MM13	16:11:25.929 ± 0.003	−51:41:57.12 ± 0.02	1.2 ± 0.1 × 0.4 ± 0.1, 50 ± 10	5.7 ± 0.6	2.7 ± 0.2	0.44 ± 0.01	⋯
MM14	16:11:25.926 ± 0.003	−51:41:58.32 ± 0.04	1.1 ± 0.1 × 0.45 ± 0.1, 160 ± 10	2.9 ± 0.2	6 ± 1	0.46 ± 0.05	⋯

Note. The masses are estimated using dust temperatures of 30 K. The final column shows the labels of the dense cores identified by Baug et al. (2021).

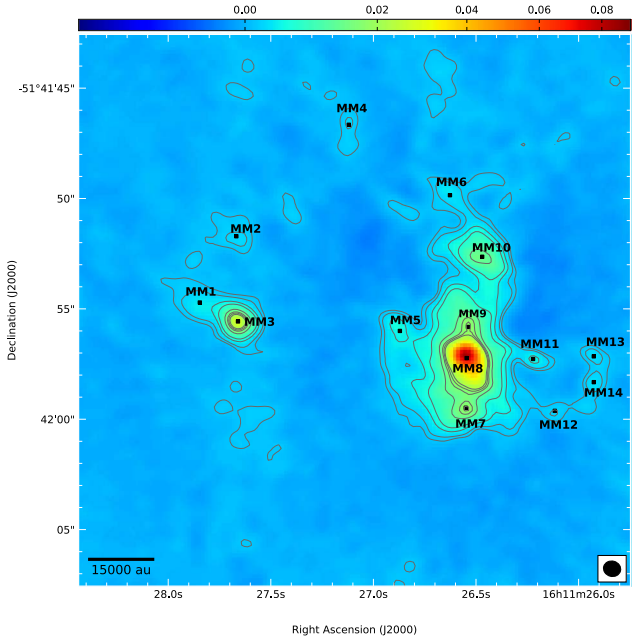

Figure 1. 0.9 mm continuum emission toward I16076 in color scale with gray contours (at 3, 5, 10, 15, 30, 40, and 45 times the rms noise level of 4 mJy beam^{-1}). The synthesized beam, shown in the bottom right corner, is $0\farcs8 \times 0\farcs7$, with PA = 74.°6. The submillimeter continuum sources identified here are marked by the black dots.

map shows that the sources are mainly distributed in two small clusters: one small cluster around MM3 and a larger one around MM8. Table 2 presents some parameters for characterizing these continuum sources, including central coordinates, deconvolved sizes, peak intensities, flux densities, and masses. These parameters—except for mass—and their uncertainties were estimated by fitting 2D Gaussians, using the CASA task `imfit`. Since the sizes of the millimeter sources are of the order of ∼0.1 pc, we assume that they correspond to dense cores.[6] MM1, MM3, MM5, MM7, MM8, and MM9 were previously identified by Baug et al. (2021), who also considered these sources as dense cores.

We calculate the masses of the dense cores using

$$M_{\rm core} = \frac{F_\nu d^2 R}{B_\nu(T_d)\kappa_\nu},$$

where F_ν is the observed total flux density, B_ν is the Planck function for a dust temperature T_d, d is the distance to the source, R is the gas-to-dust mass ratio, and k_ν is the dust opacity, which depends on the frequency as $\kappa_\nu = \kappa_o \cdot (\nu/\nu_o)^\beta$. We assume that the dust emission is isothermal and optically thin, and neglect any possible effects produced by scattering. Therefore, all the masses presented should be considered as lower limits. We adopt the same assumptions as in Fernández-López et al. (2021), who studied the massive star-forming region G 5.89-0.39, also associated with an explosive dispersal outflow. Hence, assuming that I16076 is a region similar to G5.89, we consider $\beta = 2.0$, a dust with thin ice mantles with 10^6 cm^{-3} density, and a gas-to-dust mass ratio of 100. Interpolating the dust opacity models of Ossenkopf & Henning (1994) to the observed wavelength, we obtain an opacity of 1.80 cm^2 g^{-1} at 0.9 mm. Since we do not have a measurement of the dust temperatures in the dense cores of I16076, we fix their mean dust temperature to $T_d = 30$ K (the measured temperature for the dense clump of I16076, as reported by Urquhart et al. 2018). The

[6] We use the nomenclature and definitions of Zhang et al. (2009), Hull et al. (2014), Bally et al. (2017) and Motte et al. (2018), who refer to clouds as 10–100 pc structures; to molecular clumps as 1 pc structures, where populations of both massive and lower-mass stars are formed; to dense cores as 0.01–0.1 pc structures forming one or a group of stars; and to protostellar envelopes as 1000 au (∼0.005 pc) structures comprising the densest parts of the dense core, inside which one or several protostars are formed.

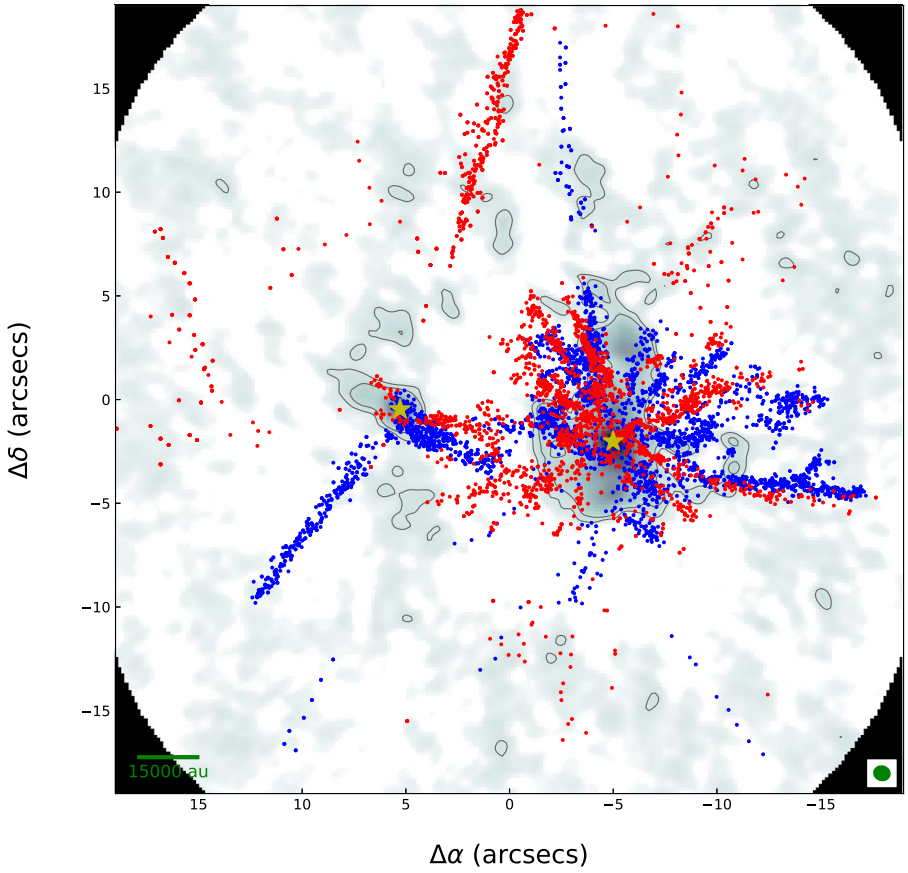

Figure 2. Image of the molecular outflows in I16076. The background gray scale image is the ALMA 0.9 mm continuum image from Figure 1, and the black contours are set at three and six times the rms noise level, respectively. The red and blue circles correspond to redshifted and blueshifted CO(3–2) gas condensation, identified in the velocity cubes as parts of the outflows in the region (see Section 3.2). The driving sources of the ensemble of filaments (west) and the blueshifted monopolar outflow lobe (east) are marked with yellow stars.

estimated masses of the dense cores range from 0.3 to 22 $M_{\odot}$ (see Table 2). To obtain the uncertainty on the masses, we only considered errors in the total observed flux density. The MM7, MM8, and MM9 cores are among the most massive, with masses greater than 10 $M_{\odot}$. The masses that we obtained are lower by a factor of 3 than the masses of the dense cores estimated by Baug et al. (2021). The reason for the discrepancies resides in the opacity, which they estimated using an expression of Hildebrand (1983), resulting in their masses being a factor of 3 higher than ours. In addition, they warned that their larger masses had to be taken with caution, as the low angular resolution could hinder multiple systems, due to their being marginally resolved. Such is the case for I16076_O1, in which we detect three possible dense cores (MM7, MM8, and MM9), and I16076_O3, composed of two dense cores (MM1 and MM3).

3.2. Outflow Identification and Kinematics

In Figure 2, we present the CO(3–2) molecular emission in the range of radial velocities from −62.15 to 83.47 km s^{-1}, avoiding the central velocity channels ([−5.5:6.2] km s^{-1}), which show extended CO emission from the cloud (velocities are expressed with respect to the cloud velocity, $v_{sys} = -87.70$ km s^{-1}).[7] We perform the identification of the outflow filaments by using Miriad's `cgcurs`[8] task (Sault et al. 1995). We manually obtain the positions and line-of-sight velocities of all half-beam (0.5 arcsec) condensations where the CO emission, in all pixels belonging to the condensation, are greater than 3σ (34 mJy beam^{-1}). Each condensation is marked with a red/blue dot, in case its velocity is redshifted/blueshifted. This procedure is repeated for each channel of the CO data cube, except for the central channels, where the cloud emission was predominant, and the channels with absorption features at 23.4 and 44.5 km s^{-1} (see Figure 3). These absorption features may be due to colder and overlapping foreground molecular clouds along the line of sight, and are beyond the scope of this contribution. In addition, the ALMA spectrum reveals other weak emission lines from other chemical species (CH_3OH, $^{34}SO_2$, HC_3N, and CH_3CHO), which are not focus of the present work. After collecting the positions of the CO(3–2) condensations, we continue to build up a map on which dozens of filament-like structures, emerging quasi-radially from a common center near the MM8 peak, can be distinguished. Two more north–south extended monopolar filaments (one blueshifted to the south and one redshifted to the north) can be seen east of the filaments associated with MM8. The blueshifted filament, with a length of ∼11″, seems to be associated with the MM3 core. The association of the northern

[7] Throughout this paper, we work with radial (or line-of-sight) velocities, v, with respect to the cloud velocity, unless otherwise noted.

[8] Cgcurs displays an image and allows the interactive reading of image values and evaluation of statistics within a polygonal region that can be interactively defined and recorded into a text file.

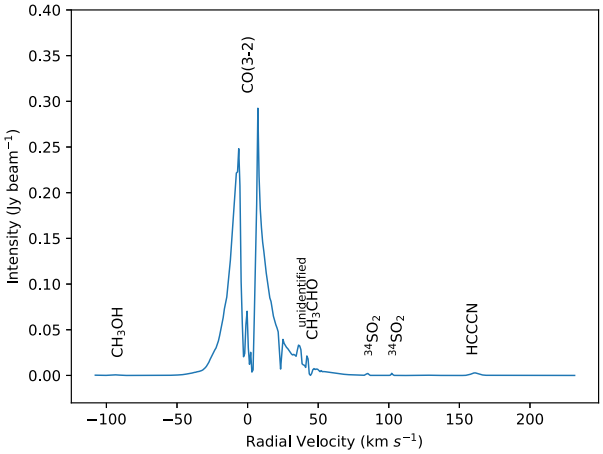

Figure 3. The CO(3–2) spectrum integrated over the whole ensemble of filaments associated with MM8. The radial velocity is expressed relative to the system cloud velocity of -87.7 km s^{-1}. The spectrum shows deep absorption by the parental cloud, but also two less prominent absorptions, at 23.4 and 44.5 km s^{-1}, which are probably due to foreground clouds along the line of sight. There are also other spectral lines (HCCCN, $^{34}SO_2$, CH_3CHO, and CH_3OH) that are much weaker than the main CO line.

redshifted filament ($\sim$18″ in length) with a dense core is not clear, although Baug et al. (2020) attribute it to the I16076_O2 core. In this work, we focus on analysis of the 24 radial filaments identified around MM8. We find 12 blueshifted and 12 redshifted filaments (see Figure 4). Most of them coincide with the outflows reported by Baug et al. (2020) and are associated with the dense core I16076_O1 (resolved into MM7, MM8, and MM9 in our work). The filament parameters, such as the terminal velocity, coordinates of the outer tip, length, and PA, are given in Table 3. Some of the filaments show very high radial velocities ($v > 50$ km s^{-1}), while others are more quiescent ($v < 10$ km s^{-1}). They show a wide range of PA values, indicating that, if they are somehow related, they do not have a preferred direction.

Figure 5 shows a diagram with the line of sight velocity as function of the projected distance (a position–velocity, or PV, diagram) of the CO molecular condensations traced by the filaments around MM8 (up to a projected distance <15″). The redshifted and blueshifted filaments are distinguished by the red and blue dots, respectively. As mentioned before, no molecular condensations were marked around 0 km s^{-1}, due to extended emission contamination. In addition, extended emission is also observed at 42.4 km s^{-1} throughout the field of view. This can be explained by the presence of other emitting clouds along the line of sight, whose extended emission is filtered by the interferometer, hindering the spatial distribution of the filaments from I16076. The CO emission from filaments at higher velocities appears to be more compact (filaments with projected lengths <2″) and close to the origin of the filaments, near the position of MM8. The black and green arrows join the central position (the peak of the MM8 core at 0 km s^{-1}) and the tips of each filament (see Table 3). The current angular resolution of the observations does not allow the kinematics of the filaments to be adequately analyzed from the PV diagram.

A 3D representation of the ensemble of the 24 CO(3–2) filaments toward I16076 gives a better idea of the isotropic morphology and its ordered kinematic pattern (Figure 6). The *X*-axis and the *Y*-axis in this graphic are the projected distance in R.A. and decl. (in arcseconds), respectively, while the *Z*-axis

Table 3
Outflow Parameters

Outflow Name	End Coordinates [R.A. (J2000)]	[Decl. (J2000)]	V_{end} (km s^{-1})	Extent (arcsec)	PA (°)
RF1	16 11 26.784	−51 41 50.28	51.36	7.6	18
RF2	16 11 26.976	−51 41 50.28	47.98	7.9	31
RF3	16 11 27.096	−51 41 52.80	49.67	7.1	50
RF4	16 11 27.768	−51 41 56.04	11.55	11.8	85
RF5	16 11 27.456	−51 42 00.00	9.86	9.3	109
RF6	16 11 27.168	−51 42 01.08	9.86	7.0	124
RF7	16 11 26.856	−51 42 01.44	54.75	5.2	146
RF8	16 11 26.208	−51 42 02.52	6.47	6.2	−150
RF9	16 11 26.352	−51 42 00.36	28.49	5.4	−131
RF10	16 11 25.320	−51 42 00.36	20.02	12.2	−106
RF11	16 11 25.968	−51 41 54.24	29.34	6.5	−62
RF12	16 11 25.992	−51 41 51.72	9.01	7.9	−43
BF1	16 11 26.736	−51 41 49.56	−19.78	8.2	13
BF2	16 11 26.880	−51 41 51.72	−33.34	6.7	30
BF3	16 11 26.928	−51 41 55.68	−44.35	4.3	68
BF4	16 11 26.760	−51 42 04.32	−14.70	7.7	164
BF5	16 11 26.304	−51 42 02.16	−18.09	5.7	−156
BF6	16 11 26.256	−51 41 59.64	−25.71	4.0	−133
BF7	16 11 25.272	−51 41 59.64	−46.04	12.5	−102
BF8	16 11 25.488	−51 41 54.96	−33.35	10.5	−77
BF9	16 11 25.800	−51 41 53.52	−12.16	8.1	−62
BF10	16 11 25.968	−51 41 52.80	−28.25	7.2	−51
BF11	16 11 26.232	−51 41 53.16	−32.49	5.3	−36
BF12	16 11 26.376	−51 41 51.72	−20.63	6.0	−16

represents the radial velocity (in km s^{-1}) of the filaments, which is also displayed by a color scale. The central position is at $(\alpha, \delta)_{J2000.0} = 16^h11^m26^s.546, -51°41'57''.23$ (the MM8 core position). For this image to represent the actual 3D distribution of the filaments, the filaments should be undergoing an expansive motion at constant velocity, following ballistic trajectories. Assuming this, Figure 6 would provide a general view of the spatial distribution and kinematics of the ensemble of filaments. As can be seen in Figures 2, 4, and 6, one of the main characteristics of the filaments is their projected quasi-isotropic distribution on the plane of the sky. They also appear to have a common origin in space and velocity. Furthermore, the velocities within most of the filaments become bluer or redder with increasing distance from the origin. This indicates that the filaments present a velocity gradient. Although a velocity gradient similar to Hubble's law is observed, this does not imply that the filaments are currently undergoing acceleration. Since no clear accelerating source is currently increasing the velocity of the filaments, these velocity gradients are likely related to the decay of the velocity of the molecular material, produced by the interactions between the filaments and the material of the environment (see Section 3.3).

3.3. Outflow Energetics

In light of the findings explained previously in Section 3.2, we hereafter assume that the ensemble of 24 radial filaments constitutes a single outflow entity with a common origin. In this section, we estimate the physical parameters of the ensemble, such as its mass, momentum, and kinetic energy. We follow an analogous procedure to that described in Fernández-López et al. (2020) for G5.89-0.39, and we consider local thermodynamic equilibrium and an optically thin CO emission. To derive the column density of the CO(3–2) transition, we use the

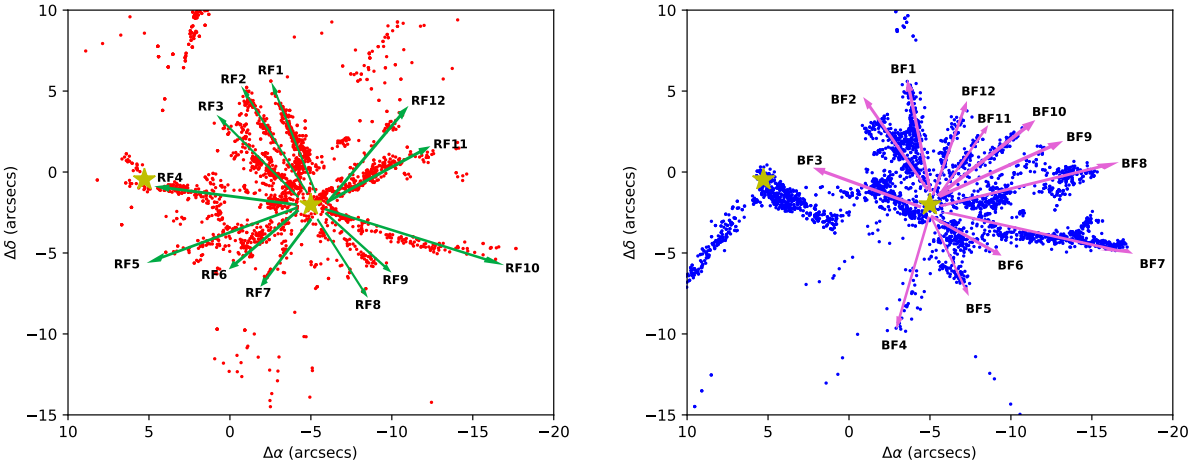

Figure 4. The redshifted (left panel) and blueshifted (right panel) CO(3–2) gas condensations detected in I16076. We identified 12 redshifted filaments and 12 blueshifted filaments, labeled RF and BF, respectively. The possible origin of the all filaments is marked with the yellow.

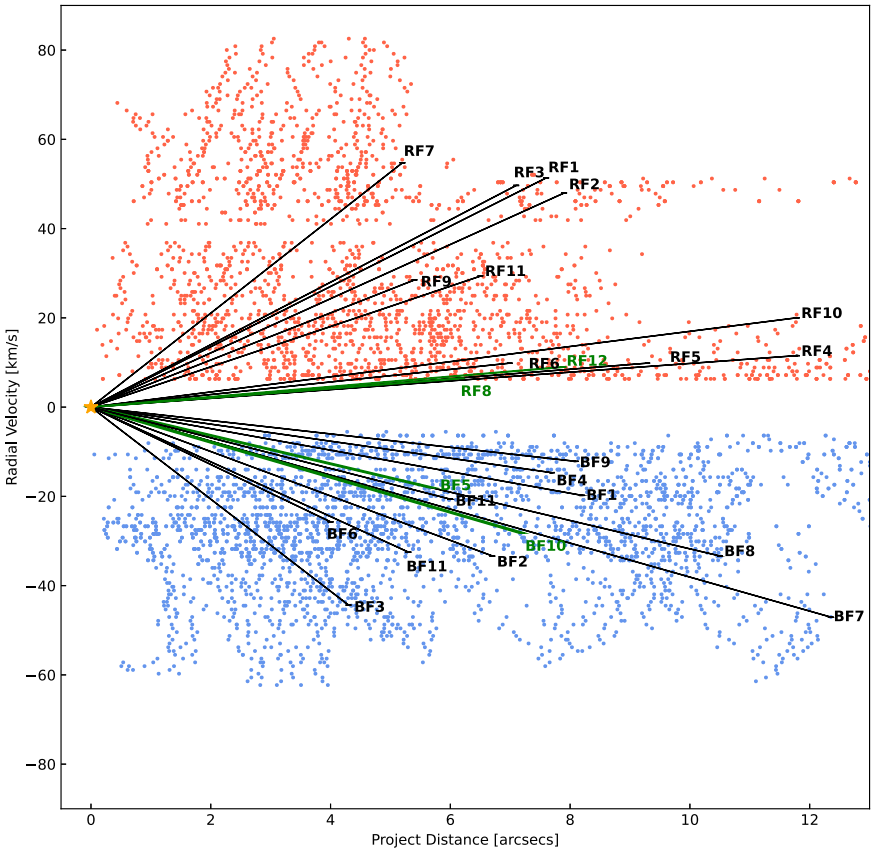

Figure 5. PV diagram of the CO(2–1) emission from the ensemble of filaments associated with I16076. The blueshifted and redshifted dots are extracted to analyze the CO condensations of the filamentary outflows emerging from the MM8 dense core. The black straight lines are plotted to link the yellow star, placed at the location of MM8 at 0 km s^{-1} (radial velocities are given with respect to the cloud velocity), and the tips of each of the 24 filaments of the ensemble. Better angular resolution is needed for better analysis of the filament kinematics.

following equation:

$$N_{\mathrm{tot}(CO)} = \frac{3\mathrm{h}}{8\pi^3 \mu_B^2 J} \cdot \frac{Q_{\mathrm{rot}}\, e^{E_u/kT_{\mathrm{ex}}}}{e^{h\nu/kT_{\mathrm{ex}}} - 1} \cdot \frac{\int T_B dv}{[J_\nu(T_{\mathrm{ex}}) - J_\nu(T_{\mathrm{bg}})]}$$
$$= \frac{1.195 \times 10^{14}(T_{\mathrm{ex}} + 0.922)e^{33.192/T_{\mathrm{ex}}}}{e^{16.596/T_{\mathrm{ex}}} - 1} \cdot \frac{T_B \Delta v}{J_\nu(T_{\mathrm{ex}}) - J_\nu(T_{\mathrm{bg}})}.$$

In the expression above, we use the Planck constant $h = 6.6261 \times 10^{-27}$ erg s; the dipole moment $\mu_B = 1.1011 \times 10^{-19}$ StatC cm; the partition function $Q_{\mathrm{rot}} = kT_{\mathrm{ex}}/(hB_0) + 1/3$, with a rigid rotor rotation constant $B_0 = 57.635968$ GHz; the quantum number of the upper level $J = 3$; the Rayleigh–Jeans equivalent temperature $J_\nu(T) = (h\nu/k)/(e^{h\nu/kT} - 1)$; the brightness temperature T_B in K; and the velocity interval Δv in km s^{-1}. Regarding the excitation temperature, we take two different values, 40K and 70 K (Felipe Navarete, private

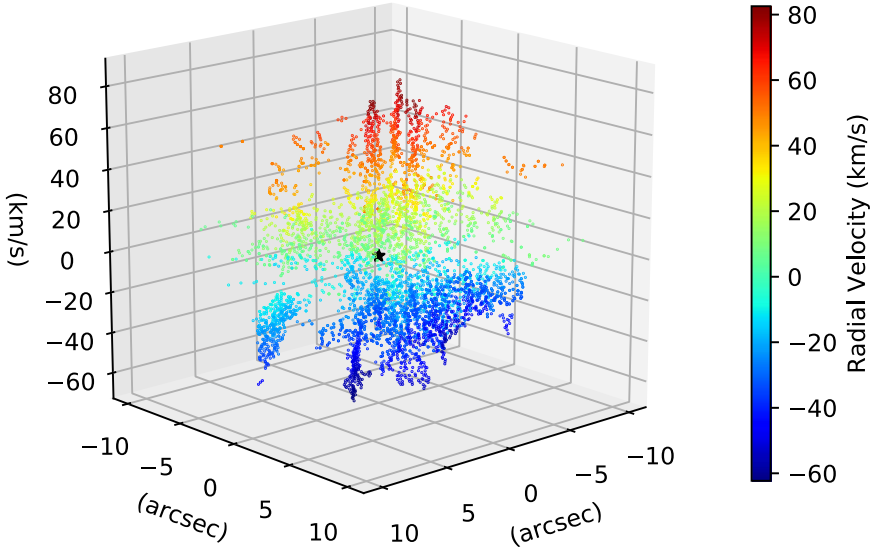

Figure 6. 3D representation of the dispersal outflowing event in I16076. The radial blueshifted and redshifted velocities are show with colors from blue to red. The LSR radial velocity scale bar (in km s^{-1}) is shown to the right. The (0″, 0″, 0 km s^{-1}) position is the origin of the plot and is marked by a black star, representing the origin of the dispersal outflow.

communication; see also Navarete et al. 2019), which are appropriate for many massive clumps in the Milky Way. We estimate the mass in each velocity channel as

$$M_{\rm out} = \mu m h \Omega N_{\rm tot} / X_{CO},$$

where μ is the mean molecular weight, which is assumed to be equal to 2.76 (Yamaguchi et al. 1999); m is the hydrogen atom mass ($\sim 1.67 \times 10^{-24}$g); Ω is the solid angle; and a CO abundance of $X_{\rm CO} = 10^{-4}$. We derive the total mass of the explosive dispersal outflow as the sum of the masses of all the filaments in each channel (see Table 3). In order not to overestimate the mass measurement, we exclude the channels that are contaminated by the emission of the parental molecular cloud and the other clouds along the line of sight, as well as the channels that are affected by other molecular line emission (CH_3CHO and unidentified) toward the wing of the CO line. Finally, we add all the channel masses to derive a total mass between 138 and 216 $M_\odot$ for 70 K and 140 K, respectively.

Recently, Raga et al. (2020) have presented an analytical "head/tail model" that could explain the kinematics found in the explosive Orion BN/KL flow. This model considers an ejected plasmon, where the tail of the plasmon decelerates due to the interaction with the medium that it passes through. The PV diagrams resulting from this model are similar to those of the Orion BN/KL filaments (Zapata et al. 2009; Bally et al. 2017), which show a velocity gradient (the radial velocity increases with the projected distance). As a first approximation, we consider a simple scenario, in which the plasmons travel with no friction. Therefore, the plasmons follow constant velocity trajectories. We also assume that the plasmons are ejected isotropically from a common origin. Therefore, the plasmons will follow a roughly constant velocity trajectory, and we also assume that they are ejected isotropically from the origin of the explosion. To better estimate the momentum and kinetic energy, it is necessary to take into account the inclination of each filament ($v_{\rm filament} = v_{\rm rad} / \cos(i)$, where $v_{\rm rad}$ is the velocity along the line of sight and i is the inclination with respect to the plane of the sky). But the resolution of the observations does not allow us to obtain information about the inclinations of each filament, so we will take the maximum observed radial velocity (83 km s^{-1}) as the expansion velocity ($V_{\rm outflow}$) of all the filaments. With this $V_{\rm outflow}$, we can estimate lower limits for the dynamic age, momentum, and kinetic energy of the outflow. We perform this analysis in Figure 7, which shows a PV diagram similar to that in Figure 5. On the PV diagram, we have superimposed models (the green curve and the shaded region) of an isotropic expansion at constant velocity, varying its dynamic age. Models of good qualitative agreement are manually found by using $t_{\rm dyn} = 3500 \pm 500$ yr. Finally, the derived total outflow are $1.2 \times 10^4\, M_\odot$ km s^{-1} and $1.8 \times 10^4\, M_\odot$ km s^{-1}, and the total outflow kinetic are 9.9×10^{48} erg and 1.5×10^{49} erg for 70 K and 140 K, respectively. This implies that the outflow emission in I16076 is associated with a very energetic event.

4. Discussion

4.1. I16076: A New Explosive Dispersal Outflow?

The outflow found in the high-mass star-forming region I16076 consists of an ensemble of at least 24 radial high-velocity filament-like ejections (ranging from −62 to +83 km s^{-1}), distributed quasi-isotropically. The filaments point back to approximately the same central position, where the MM8 dense core is located (Figure 2). Spatial overlap of the redshifted and blueshifted filaments is observed. The filaments present a linear velocity gradient (see Figure 6). In addition, the estimated energy of the filament ensemble is at least one to two orders of magnitude larger than the typical energies of outflows that are associated with high-mass protostars. All these features point to a direct analogy with those of explosive dispersal outflows: Orion BN/KL, DR21, and G5.89-0.39 (e.g., Bally 2016; Zapata et al. 2017, 2020). The collected evidence strongly suggests that I16076 is a new explosive dispersal outflow candidate. Therefore, the ejection of the filaments would have occurred from a single brief energetic event. However, new and more sensitive observations at higher angular resolution will be needed to confirm this.

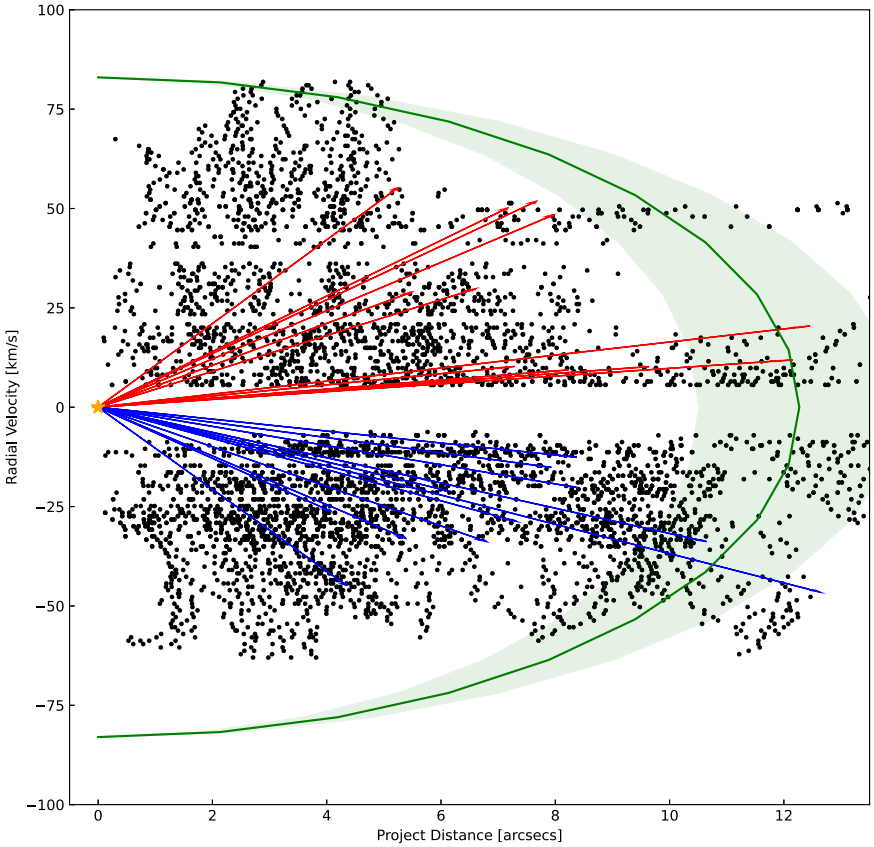

Figure 7. Models (the green curve and shaded region) of good qualitative agreement with an isotropic expansion at constant velocity ($V_{\rm outflow} = 83$ km s^{-1}) on the PV diagram, setting $t_{\rm dyn} = 3500 \pm 500$ yr.

4.2. The Rate of Explosive Dispersal Outflows in the Milky Way

As indicated by the elements explained in Section 4.1, the ensemble of filaments in I16076 could constitute a new explosive dispersal outflow. The discovery of another such dispersal event could have further implications, which we explore in this section. For instance, we have no accurate knowledge of how common these dispersal outflows are in our Galaxy , whether they play a role in the energy budget of the or the physical processes from which they originate. Figure 8 shows the spatial distribution of the currently confirmed dispersal outflows in the Milky Way, including I16076 (the red crosses). S106 IR,[9] a recently reported possible explosive dispersal outflow (the inverted blue triangle; Bally et al. 2022), is also included in the sample. Making a crude estimate, Zapata et al. (2020) derived a frequency rate of one explosive dispersal event every 130 yr in the Milky Way, considering Orion BN/KL, DR21, and G5.89-0.39. Assuming that I16076 and S106 IR are explosive dispersal outflows, we can refine this estimated rate. First, we assume that the explosive dispersal outflows are evenly spaced over time during the last 15,330 yr (this is the period of time covering all five outflows, taking into account their different distances to Earth). Second, the dispersal outflows are within a projected circle of 5.6 kpc in diameter (the separation between I16076 and DR21, the pair of known dispersal outflows that are the most separated). Finally, we extrapolate the frequency rate to the disk of the our which we assume to be a flat disk with a 15 kpc radius. Since the star formation rate is fairly constant with galactocentric distance (e.g., Nakanishi & Sofue 2006; Urquhart et al. 2014), and we only have a few explosive outflow cases, the frequency rate obtained will be a crude rate of the first-order approximation. Under these assumptions, the estimate of the frequency of the dispersal outflows in the Milky Way should be regarded as a lower limit. In this manner, we obtain a rate of one dispersal outflow every 110 yr. This frequency rate could be even larger, with the availability of a more complete high-resolution and high-sensitivity survey (not just targeted observations), which might lead to the identification of more explosive events within the considered radius.

It is worth noting that this frequency rate is comparable to the rate of supernovae (one every 50 yr; Diehl et al. 2006). This fact may have implications for the energy budget of the our even accounting for the lower amount of energy (10^{49} erg), by $\sim$100 times, that a dispersal outflow deposits in the compared with a core-collapse supernovae, which releases energies of 10^{51} erg (Hamuy 2003). The origins of explosive dispersal outflows are probably associated with the disruption of a massive young nonhierarchical stellar system and/or with a protostellar collision (Zapata et al. 2009; Bally et al. 2011; Zapata et al. 2013; Rivilla et al. 2014; Bally 2016; Bally et al. 2017). One of the consequences is the ejection of a small group of runaway protostars (e.g., Gómez et al. 2008; Rodríguez et al. 2020). Hence, there seems to be a link between the origins of explosive dispersal outflows and stellar dynamical interactions. The rate of the explosive dispersal outflows would suggest that dynamical interactions and stellar collisions may be common

[9] This region has a complex of H_2 and N[III] compact structures, with increasing proper motions with projected distance from the young high-mass stellar object, but the natures of these features still need further confirmation.

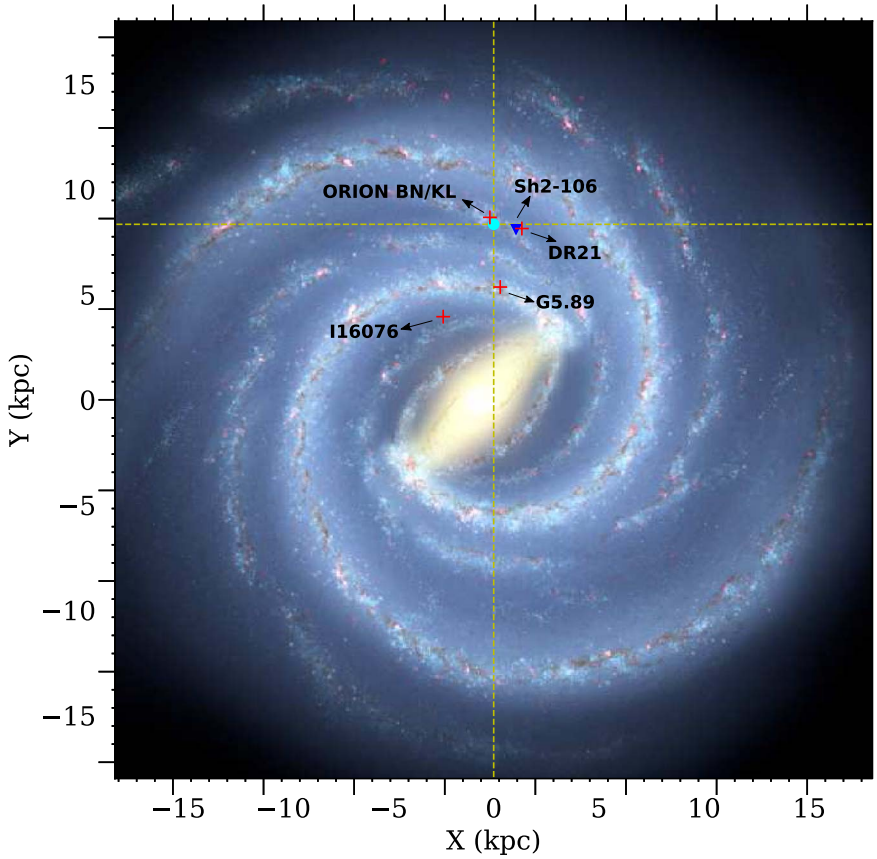

Figure 8. Sketch of the projected spatial distribution of the confirmed explosive dispersal outflows (red crosses), plus S106 IR (blue inverted triangle; Bally et al. 2022) in the Milky Way (artist's concept, R. Hurt: NASA/JPLCaltech/Spitzer Science Center). The location of the Sun is marked with the circle at the crossing of the two dashed lines.

scenarios in high-density clusters that eject runaway stars. Hence, a more complete survey of these kinds of outflows may be important in advancing our understanding of how massive stars form.

5. Conclusions

In this paper, we have presented archival observations of the 0.9 mm continuum and CO(3–2) spectral line emission toward the massive star-forming region I16076, carried out with ALMA. We found 14 dense cores associated with two small clumps. The cores have masses ranging from 0.3 to 22 $M_{\odot}$. We found an ensemble of 24 radial filament-like ejections of CO(3–2) line emission (12 blueshifted and 12 redshifted), ranging from -62.15 to $+83.47\,\mathrm{km\,s^{-1}}$, with respect to the cloud velocity ($-87.7\,\mathrm{km\,s^{-1}}$). These filaments apparently emerge from the neighborhood of the dense core MM8. Also, we reported two more extended north–south monopolar outflows, one being blueshifted, associated with MM3, and one being redshifted, launched from an unidentified source.

We analyzed the CO(3–2) morphology and kinematics of the filament ensemble around MM8. The size of the ensemble of filaments is $\sim 20''$, and each of the filaments are distributed in a radial fashion, quasi-isotropically, around a common center located close to the peak emission of MM8. The radial velocity of the filaments shows a velocity gradient. The velocity increases further away from the common center, as occurs with the fragments of an explosion. Using the integrated CO(3–2) emission, we calculated a total mass for the filaments between 138 and 216 $M_{\odot}$. Assuming an isotropic expansion model, with a constant velocity of $83\,\mathrm{km\,s^{-1}}$ and a dynamical age of 3500 yr, we derive a rough estimate for the momentum and kinetic energy of the gas of the ensemble of filaments. The order of magnitude of the kinematic energy is $10^{48\text{-}49}$ erg. Based on the evidence, we suggest that the ensemble of filaments in I16076 constitutes an explosive dispersal outflow candidate. Under this hypothesis, we made a raw estimate of the lower limit of the rate of dispersal outflows in the our considering a constant star formation rate and efficiency, with respect to the galactocentric radio of the Milky Way The value obtained is comparable to the rate of supernova explosions, which may have further implications on the role of the energy balance of the dispersal outflows in the Interstellar Medium, as well as the and of of outflow in massive star formation.

This paper makes use of the following ALMA data: ADS/JAO.ALMA#2017.1.00545.S. ALMA is a partnership of ESO (representing its member states), NSF (USA), and NINS (Japan), together with NRC (Canada) and NSC and ASIAA (Taiwan), in cooperation with the Republic of Chile. The Joint ALMA Observatory is operated by ESO, AUI/NRAO, and NAOJ. We thank the anonymous referee for the valuable comments and suggestions that helped to improve the manuscript. E.G.C. acknowledges financial support from CONACyT grant No. 280775 and is grateful for the hospitality of IRyA (CONACIT), Morelia, Mexico. T.B. acknowledges support from the S. N. Bose National Centre for Basic Sciences, under the Department of Science and Technology, Government of India.

ORCID iDs

Estrella Guzmán Ccolque https://orcid.org/0000-0003-2630-3774
Manuel Fernández-López https://orcid.org/0000-0001-5811-0454
Luis A. Zapata https://orcid.org/0000-0003-2343-7937
Tapas Baug https://orcid.org/0000-0003-0295-6586

References

Arce, H. G., Shepherd, D., Gueth, F., et al. 2007, in Protostars and Planets V, ed. B. Reipurth, D. Jewitt, & K. Keil (Tucson, AZ: Univ. Arizona Press), 245
Bally, J. 2016, ARA&A, 54, 491
Bally, J., Chia, Z., Ginsburg, A., et al. 2022, ApJ, 924, 50
Bally, J., Cunningham, N. J., Moeckel, N., et al. 2011, ApJ, 727, 113
Bally, J., Ginsburg, A., Arce, H., et al. 2017, ApJ, 837, 60
Bally, J., Ginsburg, A., Silvia, D., & Youngblood, A. 2015, A&A, 579, A130
Bally, J., & Zinnecker, H. 2005, AJ, 129, 2281
Baug, T., Wang, K., Liu, T., et al. 2020, ApJ, 890, 44
Baug, T., Wang, K., Liu, T., et al. 2021, MNRAS, 507, 4316
Bronfman, L., Nyman, L. A., & May, J. 1996, A&AS, 115, 81
Diehl, R., Halloin, H., Kretschmer, K., et al. 2006, Natur, 439, 45
Faúndez, S., Bronfman, L., Garay, G., et al. 2004, A&A, 426, 97
Fernández-López, M., Sanhueza, P., Zapata, L. A., et al. 2021, ApJ, 913, 29
Fernández-López, M., Zapata, L. A., Rodríguez, L. F., et al. 2020, AJ, 159, 171
Gómez, L., Rodríguez, L. F., Loinard, L., et al. 2008, ApJ, 685, 333
Hamuy, M. 2003, ApJ, 582, 905
Hildebrand, R. H. 1983, QJRAS, 24, 267
Hull, C. L. H., Plambeck, R. L., Kwon, W., et al. 2014, ApJS, 213, 13
Konigl, A., & Pudritz, R. E. 2000, in Protostars and Planets IV, ed. V. Mannings, A. P. Boss, & S. S. Russell (Tucson, AZ: Univ. Arizona Press), 759
Liu, T., Evans, N. J., Kim, K.-T., et al. 2020, MNRAS, 496, 2821
Liu, T., Kim, K.-T., Yoo, H., et al. 2016, ApJ, 829, 59
Motte, F., Bontemps, S., & Louvet, F. 2018, ARA&A, 56, 41
Nakanishi, H., & Sofue, Y. 2006, PASJ, 58, 847
Navarete, F., Leurini, S., Giannetti, A., et al. 2019, A&A, 622, A135
Ossenkopf, V., & Henning, T. 1994, A&A, 291, 943
Peng, T. C., Zapata, L. A., Wyrowski, F., Güsten, R., & Menten, K. M. 2012, A&A, 544, L19
Raga, A. C., Rodríguez-González, A., Hernández-Martínez, L., Cantó, J., & Castellanos-Ramírez, A. 2020, MNRAS, 499, L91
Rivera-Ortiz, P. R., Rodríguez-González, A., Cantó, J., & Zapata, L. A. 2021, ApJ, 916, 56
Rivilla, V. M., Jiménez-Serra, I., Martín-Pintado, J., & Sanz-Forcada, J. 2014, MNRAS, 437, 1561
Rodríguez, L. F., Dzib, S. A., Zapata, L., et al. 2020, ApJ, 892, 82
Sault, R. J., Teuben, P. J., & Wright, M. C. H. 1995, in ASP Conf. Ser., 77, Astronomical Data Analysis Software and Systems IV, ed. R. A. Shaw, H. E. Payne, & J. J. E. Hayes (San Francisco, CA: ASP), 433
Shu, F. H., Adams, F. C., & Lizano, S. 1987, ARA&A, 25, 23
Shu, F. H., Najita, J. R., Shang, H., & Li, Z. Y. 2000, in Protostars and Planets IV, ed. V. Mannings, A. P. Boss, & S. S. Russell (Tucson, AZ: Univ. Arizona Press), 789
Shu, F. H., Ruden, S. P., Lada, C. J., & Lizano, S. 1991, ApJL, 370, L31
Urquhart, J. S., Figura, C. C., Moore, T. J. T., et al. 2014, MNRAS, 437, 1791
Urquhart, J. S., König, C., Giannetti, A., et al. 2018, MNRAS, 473, 1059
Wenger, T. V., Balser, D. S., Anderson, L. D., & Bania, T. M. 2018, ApJ, 856, 52
Wood, D. O. S., & Churchwell, E. 1989, ApJ, 340, 265
Yamaguchi, R., Akira, M., & Yasuo, F. 1999, in Star Formation 1999, ed. T. Nakamoto (Nagano: Nobeyama Radio Observatory), 383
Zapata, L. A., Ho, P. T. P., Fernández-López, M., et al. 2020, ApJL, 902, L47
Zapata, L. A., Ho, P. T. P., Guzmán Ccolque, E., et al. 2019, MNRAS, 486, L15
Zapata, L. A., Schmid-Burgk, J., Ho, P. T. P., Rodríguez, L. F., & Menten, K. M. 2009, ApJL, 704, L45
Zapata, L. A., Schmid-Burgk, J., Pérez-Goytia, N., et al. 2013, ApJL, 765, L29
Zapata, L. A., Schmid-Burgk, J., Rodríguez, L. F., Palau, A., & Loinard, L. 2017, ApJ, 836, 133
Zhang, Q., Wang, Y., Pillai, T., & Rathborne, J. 2009, ApJ, 696, 268